

Influence of a Prior Oxidation on the Reduction Behavior of Magnetite Iron Ore Ultra-Fines Using Hydrogen



THOMAS WOLFINGER, DANIEL SPREITZER, HENG ZHENG,
and JOHANNES SCHENK

The reduction behavior of raw and prior-oxidized magnetite iron ore ultra-fines with hydrogen was investigated. Reduction tests were conducted with a thermogravimetric analyzer in a temperature range from 873 K to 1098 K at 1.1 bar absolute, using hydrogen as reducing gas. The experimental results show that a prior oxidation of the magnetite has a positive effect on the reduction behavior because of changing morphology. The apparent activation energies show a turnaround to negative values, depending on the prior oxidation and degree of reduction. A multi-step kinetic analysis based on the model developed by Johnson–Mehl–Avrami was used to reveal the limiting mechanism during reduction. At 873 K and 948 K, the reduction at the initial stage is controlled by nucleation and chemical reaction and in the final stage by nucleation only, for both raw and pre-oxidized magnetites. At higher temperatures, 1023 K and 1098 K, the reduction of raw magnetite is mainly controlled by diffusion. This changes for pre-oxidized magnetite to a mixed controlled mechanism at the initial stage. Processing magnetite iron ore ultra-fines with a hydrogen-based direct reduction technology, lower reduction temperatures and a prior oxidation are recommended, whereby a high degree of oxidation is not necessary.

<https://doi.org/10.1007/s11663-021-02378-1>
© The Author(s) 2021

I. INTRODUCTION

THE iron and steel industry is one of the biggest single emitters of CO₂ emissions, accounting for one third of the global industrial CO₂ emissions.^[1–4] The conventional ore-based iron- and steelmaking production route, blast furnace and basic oxygen furnace, emits in the range of 1700 to 1900 kg of CO₂ per ton of liquid steel.^[4,5]

As pointed out by ecological evaluations of steel production technologies, a promising and attractive route is the hydrogen-based direct reduction in combination with an electric arc furnace.^[1–4,6] Using natural gas as a basis for the reducing gas, CO₂ emissions can be

halved compared to those emitted from the blast furnace and basic oxygen furnace.^[5] A further reduction is achievable using hydrogen generated from electrolysis with renewable energies towards 100 to 250 kg of CO₂ per ton of liquid steel.^[4]

Besides the trend of lowering the CO₂ emissions, new innovative ore-based iron- and steel production technologies must be able to process any type of iron oxide in the form of ultra-fines due to their steadily increasing availability. This trend of an increasing production of ultra-fine iron ore is due to mining and intensive beneficiation of low-grade ore deposits, especially magnetite, because high-grade lumpy ore resources are becoming depleted.^[7] Using iron ore ultra-fines directly, a further decrease in energy consumption and CO₂ emissions is achievable because of the omission of the agglomeration process (*e.g.* pelletizing).^[1,2,8] A suitable technology for the direct usage of fine materials without prior agglomeration is the fluidized bed technology.^[9,10] Proven industrial-scale fluidized bed processes for the direct usage of fine iron ore are the Finmet[®], Circored[®] and the pre-reduction sequence of the Finex[®] process.^[9–13] Therefore, a direct reduction process based on the fluidized bed technology to process all types of iron oxides in the form of ultra-fines using only hydrogen as reducing gas seems to be a promising solution for a low-carbon economy. The use of

THOMAS WOLFINGER and JOHANNES SCHENK are with the K1MET GmbH, Stahlstraße 14, 4020 Linz, Austria and also with the Chair of Ferrous Metallurgy, Montanuniversität Leoben, FranzJosefstraße 18, 8700 Leoben, Austria. Contact e-mail: thomas.wolfinger@k1-met.com DANIEL SPREITZER is with the Primetals Technologies Austria GmbH, Turmstraße 44, 4020 Linz, Austria. HENG ZHENG is with the Chair of Ferrous Metallurgy, Montanuniversität Leoben.

Manuscript submitted June 24, 2021; accepted October 17, 2021.

Article published online December 21, 2021.

hydrogen as reducing agent requires a pre-heating of the iron ore to balance the endothermic character of the hydrogen-based reduction. In the case of magnetite, this pre-heating can be done *via* a gas with a remaining amount of oxygen to utilize the exothermic oxidation reaction from Fe_3O_4 to Fe_2O_3 . Though, the same amount of the generated energy due to the oxidation is needed for the reduction afterwards. Therefore, the focus has to lay on a facilitation of the reduction kinetic. As a result, a lower overall energy consumption of the process is potentially achievable.

The main difficulty for a direct reduction process based on the fluidized bed technology is to keep the fluidization stable due to the changing surface morphology of the iron ore particles, as reported by several authors.^[14–26] Moreover, the formation of a dense iron layer around the particles leads to particularly long reduction times.^[15,23,27,28]

To avoid the fluidization issue and focus only on the morphological changes during the reduction process, a thermogravimetric analyzer (TGA) was chosen for this study. The scope of this work was to investigate the effect of a prior oxidation of magnetite ultra-fines on the morphology and thus reduction kinetics using hydrogen as reducing agent. Proper process conditions for a possible novel industrial-scale direct reduction process shall be deduced from the results. The reduction kinetics was analyzed by means of a multi-step kinetic analysis, based on the model developed by Johnson–Mehl–Avrami. The change in the controlling mechanisms with the reduction degree is discussed along with the prevailing iron morphology.

II. EXPERIMENTAL

A. Materials

Three samples were used in this work; one raw and two pre-oxidized magnetite iron ore ultra-fines with different degrees of oxidation (ODs), 53 and 90 pct. For the oxidizing pre-treatment of the magnetite iron ore ultra-fines, a conventional heat treatment furnace using a temperature of 1023 K for a defined oxidation time, t_i , was used. About 0.4 kg of the raw magnetite ultra-fines were charged into a 250×350 mm vessel to maintain only a small bed height of approx. 2.5 mm, avoiding any inhomogeneous areas during oxidation. The furnace chamber volume of 130 dm^3 filled with air ensures enough oxygen for the oxidation. The achieved degrees of oxidation (ODs) of 53 and 90 pct were calculated according to the mass balance before, m_0 , and after, m_i ; the oxidation treatment was divided by the theoretically possible oxygen up-take by the iron oxide according to the chemical analysis, as given by the following equation:

$$\text{OD}_i = \frac{m_i - m_0}{m_0 * \text{wtpctFeO} * (M_{\text{Fe}_2\text{O}_3}/2 * M_{\text{FeO}} - 1)} * 100\text{pct} \quad [1]$$

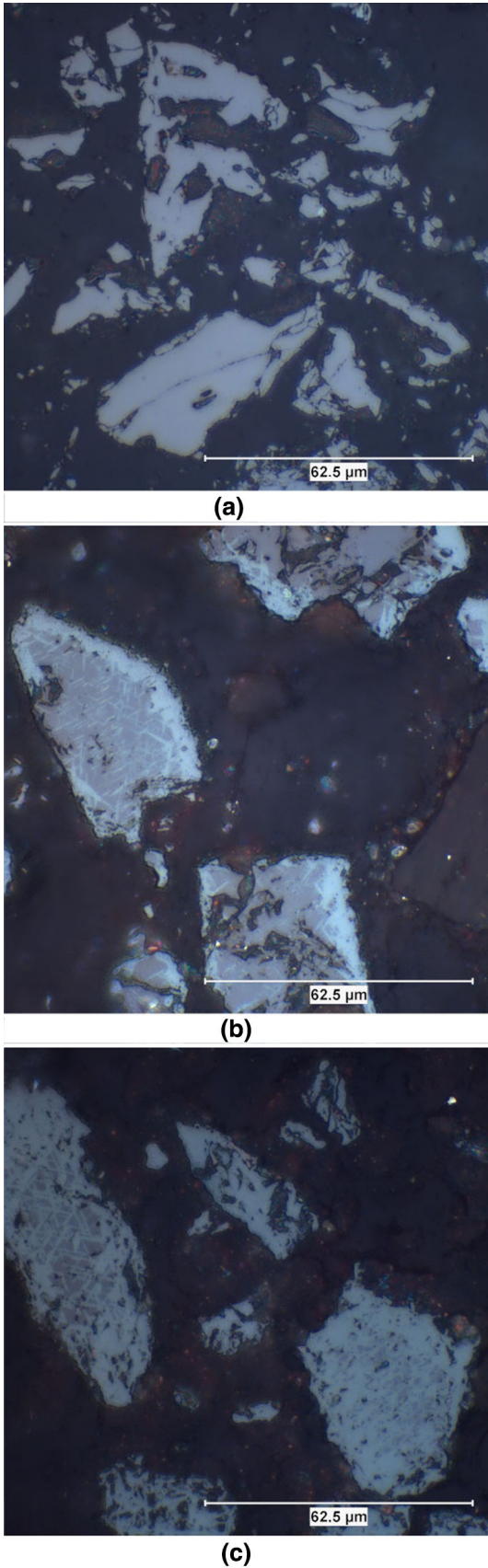
where M_{FeO} and $M_{\text{Fe}_2\text{O}_3}$ are the molar weight masses of wüstite and hematite, respectively.

In Figure 1, optical microscope images of the raw and oxidized ultra-fines are presented. Denser areas appears brighter under the optical microscope, which indicates oxidized magnetite.^[29–35] The raw magnetite appears to be dense iron ore, as given in Figure 1(a). The conversion due to the oxidation of the magnetite ultra-fines follows a plate-like growth from the outer surface towards the core, as illustrated with the white areas in Figures 1(b) and (c) for the 53 and 90 pct oxidized magnetite. This structure characteristics of oxidized magnetite is also reported form other authors.^[29,35,36]

The chemical analysis of the raw magnetite and the bulk material data of the raw and oxidized ultra-fines are given in Table I. The chemical analysis was conducted by titration for the iron species and for the gangue elements, by X-ray fluorescence analysis. According to the laser diffraction measurement (CILAS type 1064 L), no significant change in the particle size distribution due to the oxidation treatment occurred, as represented by the characteristic diameters D_{20} , D_{50} , and D_{80} in Table I. A characteristic diameter D_{50} means that 50 vol pct of the bulk material has a diameter less than this value. Consequently, the oxidation at 1023 K does not lead to any kind of particle agglomeration, which can be also confirmed by the optical microscope images displayed in Figure 1. The specific surface, measured according to B.E.T. (TriStar II 3020 micromeritics using 30 pct N_2 in He), decreases significantly and the apparent density, measured with a helium pycnometer (Quantachrome Ultrapycnometer 1000), increases slightly with an increasing degree of oxidation. Forsmo *et al.* explained this phenomenon as a result of the sintering effect and of the contraction of the magnetite during the oxidation.^[37]

B. Apparatus and Procedure

The schematic concept of the thermogravimetric analyzer used for the reduction experiments is shown in Figure 2. The testing facility mainly consists of the reactor chamber with an electrical heating system, the weighing system, and the gas supply system including gas pre-heating and a humidifier. The gas flow rates of inert gas and reducing gas are controlled by mass flow controllers (Bronkhorst MFC F-201CV). Pre-heating of the gas takes place before entering the reactor from the bottom. Inside the reaction chamber, the sample basket filled with iron ore ultra-fines is positioned and kept at the defined temperature by a PID controller driven by a thermocouple (type N) placed directly beneath the sample basket. The sample basket has a diameter of 1 cm, a height of 5 cm and is made of two overlapping layers of a stainless-steel mesh with a mesh size of $64 \mu\text{m}$. The reason for this is to allow the gas to flow through the ore sample from all sides but prevent the ore from falling through the mesh, thus avoiding the limitation due to gas diffusion through the bulk material. A similar sample basket was also used by Fruehan *et al.*^[14] The sample basket is positioned inside a silica tube and fixed to the weighing system (Sartorius Micro M 25 D-P), which is a micro beam scale with a



◀ Fig. 1—Images of polished microsections of the magnetite-based iron ore ultra-fines used: (a) raw, (b) 53 pct oxidized, (c) 90 pct oxidized.

measuring range of -100 mg to $+1000$ mg and an accuracy of 0.1 mg. The weight of the ore sample, all gas flow rates, temperatures, and the system pressure inside the apparatus are recorded *in situ* during the experiment.

For each experiment, 2.5 g of iron ore were charged into the sample basket which was connected to the weighing system and positioned inside the reaction chamber. After that, the gas supply system and the reactor chamber—including the sample—were heated up under inert atmosphere (nitrogen, Linde Germany, purity 99.999 vol pct). At the defined temperature, the inert atmosphere was changed to the reducing atmosphere (hydrogen, Linde Germany, purity 99.999 vol pct) for a defined time and afterwards, a cooling under inert atmosphere took place. After cooling, polished microsections of the reduced samples were further analyzed by an optical light microscope (Polivar Reichert-Jung MEF2).

C. Experimental Conditions

The reduction of hematite Fe_2O_3 by hydrogen to metallic iron Fe at temperatures above 843 K proceeds *via* magnetite Fe_3O_4 to wüstite FeO. Below 843 K, only magnetite is involved in the reduction sequence, as given by the equations in Figure 3, the Baur–Glässner diagram for the Fe–O– H_2 system.^[38] In this diagram, the stability areas of different iron oxides as a function of the temperature are illustrated on the ordinate and the gas mixture on the abscissa. The thermodynamic data for the calculation was taken from FactSageTM 7.3 (Database: FactPS, FToxide).

The testing conditions for the reduction test campaign of the iron ore ultra-fines are exhibited in Table II. Due to the high flow rate and small sample amount, the reduction temperature remained constant for the whole experiment despite the endothermic character of the hydrogen reduction of iron oxides.

III. RESULTS AND DISCUSSION

A. Experimental Results

To compare the experimental results, the measured weight loss curve against time due to the oxygen removal during the reduction needs to be converted into the degree of reduction (RD) according to the following equation^[9]:

$$\text{RD} = \left(1 - \frac{O}{1.5\text{Fe}_{\text{tot}}} \right) \quad [2]$$

where O stands for the total amount of oxygen bonded on iron in mol and Fe_{tot} for the total amount of iron in the sample in mol. The starting value for RD is given by the chemical analysis, whereby a RD of 0 pct represents Fe_2O_3 , 11.1 pct Fe_3O_4 , 33.3 pct FeO, and 100 pct a complete transformation to Fe.

Figure 4 shows the degree of reduction against time for the raw and oxidized magnetites at the four different reduction temperatures used, where the light gray lines represent the experimental curves and the black lines demonstrate the fitted curves. The fitted curves are obtained from the kinetic evaluation, which will be explained in the next section. It can be seen that the pre-oxidation significantly favors the reduction. Especially for the later stage of the reduction at the higher temperatures 1023 K and 1098 K, an improvement in the reduction can be observed in the case of a prior oxidation. Without prior oxidation, the deceleration of the reduction rate starts at a degree of reduction between 35 and 50 pct, as given in Figure 4(a). This flattening behavior is still given for the pre-oxidized magnetites, but at a higher degree of reduction of 85 and 75 pct for 1023 K and 1098 K, respectively, displayed in Figures 4(b) and (c). At 948 K, the effect of the pre-oxidation shows a minimum, represented by the close course of the degree of reduction for all three materials. For the reduction temperature of 873 K, the influence of the pre-oxidation is significant again by means of a faster reduction. In contrast to high reduction temperatures, an almost complete reduction for all three materials was achieved at lower reduction temperatures of 873 K and 948 K.

From a thermodynamic point of view, higher temperatures increase the reduction rate due to the expanding stability area of iron, as shown in Figure 3. This correlation can only be seen for the experimental results in Figure 4 at the initial stage of the reduction. For the final stage of the reduction for experiments at higher temperatures, the course of the degree of reduction flattens at lower RDs compared to lower reduction temperatures. This indicates a change in the kinetic limitations and morphology.

Comparing the bulk material properties, the expected reduction rate of the oxidized magnetites would be lower compared to the raw magnetite because of the lower porosity.

The reduction rate benefits from the high initial porosity of the iron ore due to the facilitated permeability of the reducing gas to the reaction interface.^[27,39,40]

Edström^[27] demonstrated that the oxidation of magnetite could promote the reduction process under certain reduction conditions. The correlation is explained by an increasing number of imperfections due to the oxidation, which accelerates the diffusion and therefore facilitates the formation of pores during the reduction. As a condition for the formation of pores, however, the reduction parameters have to be set adequately for the iron ore.

Pineau^[6] and Kim^[15] identified similar results to those of this study; a lower reduction rate for the reduction of magnetite fines at temperatures around 1023 K and 1098 K compared to 873 K and 948 K.

By means of the effect of a pre-oxidation on the reduction behavior of magnetite iron ore ultra-fines with hydrogen, a map can be drawn, based on the experimental results in Figure 4, as illustrated in Figure 5. The time needed to achieve a reduction degree of 65, 85, or 95 pct is plotted as a function of the degree of oxidation and reduction temperature as a surface. For plotted data above the experimental reduction time of 1200 seconds, an interpolation based on the reduction rate at the final reduction stage was applied.

B. Evaluation of the Apparent Activation Energy Using the Model-Free Method

The reduction rate for isothermal gas-solid reactions is obtained using the first deviation on the conversion X plotted over time, as given in Eq. [3]^[39–41]:

$$\frac{dX}{dt} = k(T) * f(X) \quad [3]$$

where $k(T)$ is the temperature-dependent reaction rate constant and $f(X)$ is the mathematical description of the reaction model based on mechanistic assumptions, as given in Table III. $f(X)$ remains constant for a particular reduction condition.

The dependence of $k(T)$ on the temperature is given by the Arrhenius equation^[41,42]:

$$k(T) = A^{-E_a/RT} \quad [4]$$

where A is the pre-exponential factor, E_a is the apparent activation energy, R is the gas constant and T is the absolute temperature. The combination of Eqs. [3] and [4] leads to Eq. [5], which enables the evaluation of E_a via its logarithmic form given in Eq. [6]. The evaluation is done by a linear regression of a $\ln(dX/dt)$ plot over temperature, also known as the Arrhenius plot, and by setting the reaction model $f(X)$ to 1.

$$\frac{dX}{dt} = A^{-E_a/RT} * f(X) \quad [5]$$

$$\ln\left(\frac{dX}{dt}\right) = -\frac{E_a}{RT} + \ln(A) + \ln[f(X)] \quad [6]$$

Figure 6 shows the reduction rates, representing dX/dt , of the experimental results of the 90 pct oxidized magnetite for different temperatures. It can be seen that at higher temperatures, the reduction rate is higher at the initial stage but decreases faster towards the final stage of reduction. At a reduction degree around 70 pct, the reduction rate for lower temperatures, 873 K and 948 K, is higher than for higher temperatures, 1023 K and 1098 K, indicating different kinetic limitations for lower and higher temperatures.

Table I. Bulk Material Properties of the Raw and Oxidized Magnetite Iron Ore Ultra-Fines

Chemical Analysis		Bulk Material Properties			
Raw Material		Raw Material	Oxidized 53 Pct OD	Oxidized 90 Pct OD	
Fe _{tot} (Pct Wt)	65.65	apparent density (g/cm ³)	4.96	5.03	5.02
FeO (Pct Wt)	27.66	D ₂₀ (pct vol)	13.1	13.8	13.5
CaO (Pct Wt)	1.62	D ₅₀ (pct vol)	33.4	35.2	34.8
MgO (Pct Wt)	1.04	D ₈₀ (pct vol)	58.8	61.1	60.4
SiO ₂ (Pct Wt)	3.33	particle size distribution (μm)	0 to 125	0 to 125	0 to 125
Al ₂ O ₃ (Pct Wt)	1.16	specific surface (m ² /g)	0.927	0.421	0.363

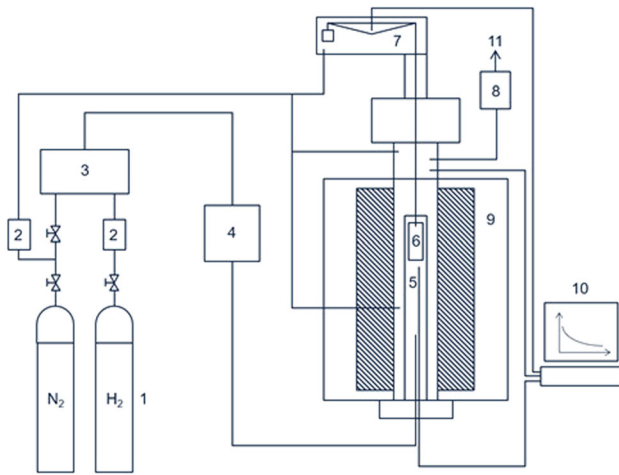


Fig. 2—Layout of the thermogravimetric analyzer: 1-gas bottles; 2-mass flow controllers; 3-gas mixing unit; 4-humidifier; 5-thermocouple; 6-sample basket; 7-beam scale; 8-pressure regulator; 9-electrical heating shell; 10-process control; 11-off-gas to atmosphere.

Table II. Testing Conditions for the Reduction Experiments

Testing Conditions	
Temperature (K)	873/948/1023/1098 K
Reducing Gas (Pct Vol)	100 pct H ₂
Inert Gas (Pct Vol)	100 pct N ₂
Pressure (Bar Absolute)	1.1
Flow Rate Reducing Gas (l min ⁻¹)*	3.5
Flow Rate Inert Gas (l min ⁻¹)*	1.5
Input Mass Iron Ore (g)	2.5
Particle Size Distribution (μm)	0 to 125

*SATP: $p = 1 \text{ atm}$, $T = 298.15 \text{ K}$.

The apparent activation energy against the degree of reduction is obtained from the linear regressions and is shown in Figure 8. As it can be seen, the course of E_a changes with the degree of reduction. The highest values of E_a are at the beginning of the reduction at 35 kJ/mol. Although, it is necessary to consider the equilibrium gas compositions, which varies with reduction temperature and reduction progress.^[24,43] This is illustrated in the Baur–Glaessner diagram in Figure 3. A fast decrease in E_a is exhibited until 12.5 pct RD, followed by a slow decrease until 60 pct RD, when the slope starts to decrease fast again. From the theoretical point of view high values for E_a are expected at the beginning of the reduction because of the equilibrium between Fe₃O₄ and FeO. This is in line with the experimental results. Negative values of E_a above 67.5 pct RD are a result of the changing slope of the linear regression lines from the Arrhenius plot in Figure 7. This is due to the differently changing reduction rates at different temperatures, indicated in Figure 6 and owing to the experimental data of Figure 4(c). Negative values of E_a mean a faster reduction at lower temperature. This phenomenon occurs when a kinetic limitation appears at a higher temperature.

By comparing the curve progression of E_a of the raw, 53 and 90 pct oxidized magnetite, the effect of a prior oxidation can be pointed out, as given in Figure 9. Both of the oxidized magnetites show a similar course, whereby the 90 pct oxidized magnetite has significantly lower values of E_a . Starting at 33 kJ/mol at 10 pct RD for the 53 pct oxidized magnetite, the 90 pct oxidized magnetite is at 30 kJ/mol. At higher degrees of reduction, the rapid decrease in E_a starts for the 53 pct

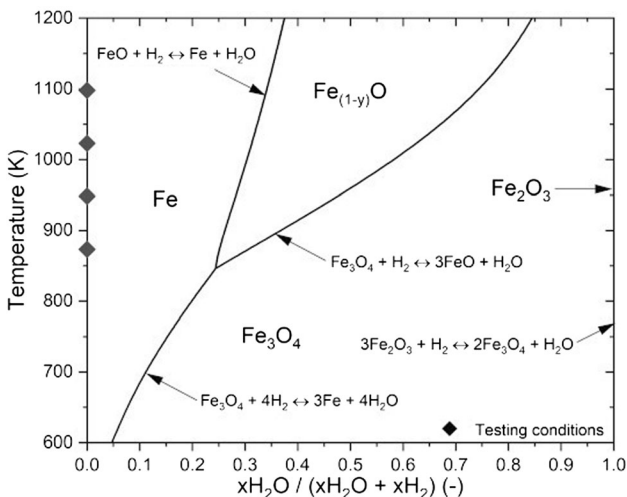


Fig. 3—Baur–Glaessner diagram for the iron oxide reduction with hydrogen including marks from of the testing conditions.

The Arrhenius plot for different degrees of reduction is presented in Figure 7, where the mathematical function $f(X)$ was set to 1, resulting in the model-free fitting method.

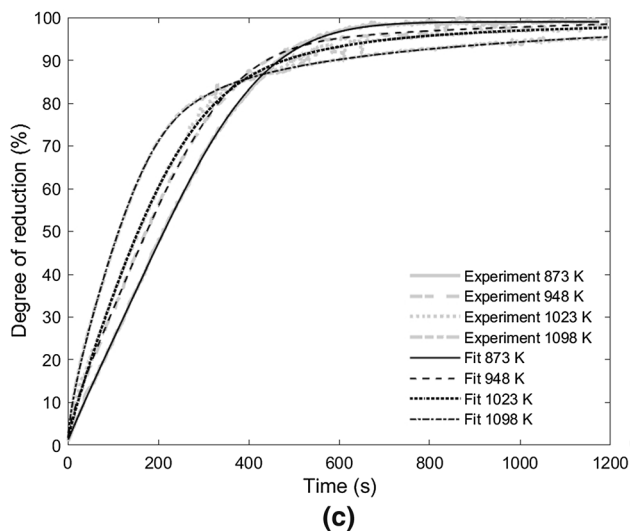
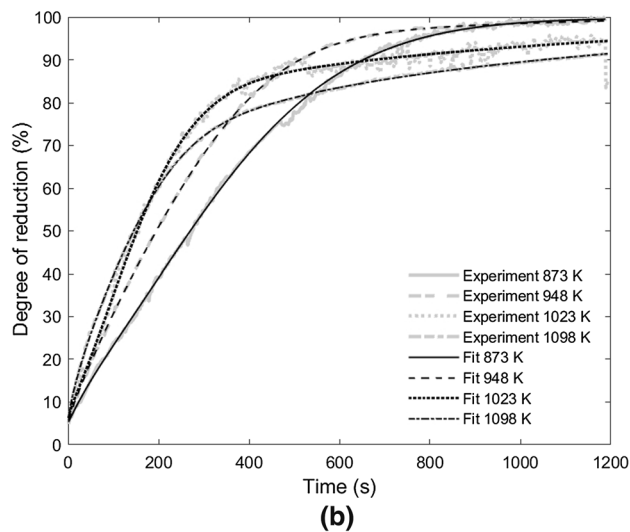
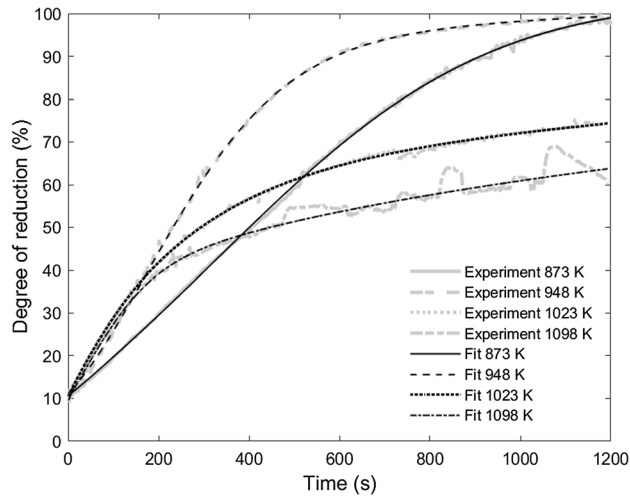


Fig. 4—Degree of reduction against time at different reduction temperatures for: (a) raw magnetite; (b) 53 pct oxidized magnetite; (c) 90 pct oxidized magnetite.

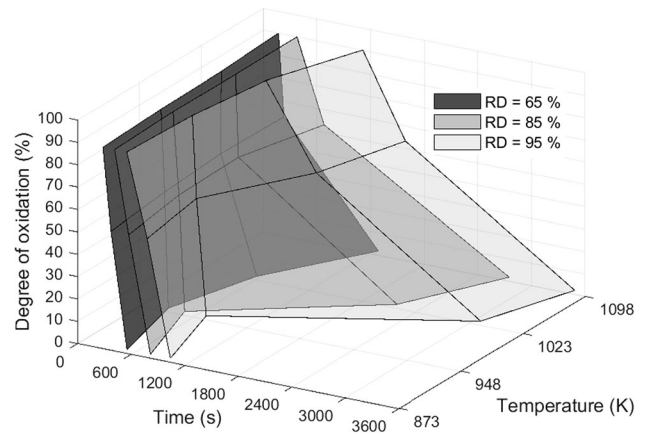


Fig. 5—Reduction performance of magnetite ultra-fine iron ore as a function of degree of oxidation and reduction temperature with interpolated data points above 1200 s.

oxidized magnetite about 10 pct of RD earlier, whereby both show negative values of E_a above 67.5 pct RD. In contrast to the oxidized magnetites, the raw magnetite has negative values of E_a at 35 pct RD. The negative values of E_a indicate that the assumption for the mathematical function $f(X)$ equal to 1 is not valid and a change in the kinetic limitation occurs during reduction. A further study of the kinetics and morphology should clarify negative values for E_a and the different trends of the samples.

IV. KINETIC EVALUATION

A. Conventional Model-Fitting Method

A straightforward approach to getting access to the predominant reaction kinetics of isothermal gas–solid reactions is using the integration of Eq. [3] in the following expression:

$$g(X) = \int_0^X \frac{dX}{f(X)} = k(T) * t \quad [7]$$

where t is the reduction time and $g(X)$ is the integral form of the reaction model, which is also given in Table III. By inserting the experimental conversion, in this case the RD, and the reduction time t into Eq. [7], the reaction mechanism can be inferred when a straight line is obtained. The higher the degree of linearity of the straight line, the better the fit. This is characterized by the coefficient of determination R^2 , where a value of 1 for R^2 indicates a straight line. This procedure is known as the conventional model-fitting method and enables information about the kinetics of the reaction according to the physical meaning behind the reaction models identified in Table III.

Figure 10 shows the results of the conventional model-fitting method from the reduction of the 90 pct oxidized magnetite at 873 K. The fitting results for each model are listed according to R^2 in the legend. It can be

Table III. Conventional Models for Gas–Solid Reactions.^[39]

Model	$f(X) = 1/k * dX/dt$	$g(X) = k * t$
Phase-Boundary Controlled/Geometrical Contraction Models		
Mass Transport (PB1)	1	X
Contracting Area (PB2)	$2 * (1 - X)^{1/2}$	$1 - (1 - X)^{1/2}$
Contracting Volume (PB3)	$3 * (1 - X)^{2/3}$	$1 - (1 - X)^{1/3}$
Diffusion Models		
1-D Diffusion (D1)	$1/(2 * X)$	X^2
2-D Diffusion (D2)	$1/[-\ln(1 - X)]$	$(1 - X) * \ln(1 - X) + X$
3-D Diffusion – Jander (D3)	$3/2 * (1 - X)^{2/3} * [1 - (1 - X)^{1/3}]$	$[1 - (1 - X)^{1/3}]^2$
3-D Diffusion – Ginstling (D4)	$3/2 * [(1 - X)^{-1/3} - 1]$	$1 - 2/3 * X - (1 - X)^{2/3}$
Reaction Order Models		
First Order (R1)	$1 - X$	$-\ln(1 - X)$
3/2 Order (R1.5)	$(1 - X)^{3/2}$	$2 * [(1 - X)^{-1/2} - 1]$
Second Order (R2)	$(1 - X)^2$	$(1 - X)^{-1} - 1$
Third Order (R3)	$(1 - X)^3$	$1/2 * [(1 - X)^{-2} - 1]$
Nucleation Models		
Avrami–Erofeev 1.5 (A1.5)	$3/2 * (1 - X) * [-\ln(1 - X)]^{1/3}$	$[-\ln(1 - X)]^{2/3}$
Avrami–Erofeev 2 (A2)	$2 * (1 - X) * [-\ln(1 - X)]^{1/2}$	$[-\ln(1 - X)]^{1/2}$
Avrami–Erofeev 3 (A3)	$3 * (1 - X) * [-\ln(1 - X)]^{2/3}$	$[-\ln(1 - X)]^{1/3}$
Avrami–Erofeev 4 (A4)	$4 * (1 - X) * [-\ln(1 - X)]^{3/4}$	$[-\ln(1 - X)]^{1/4}$

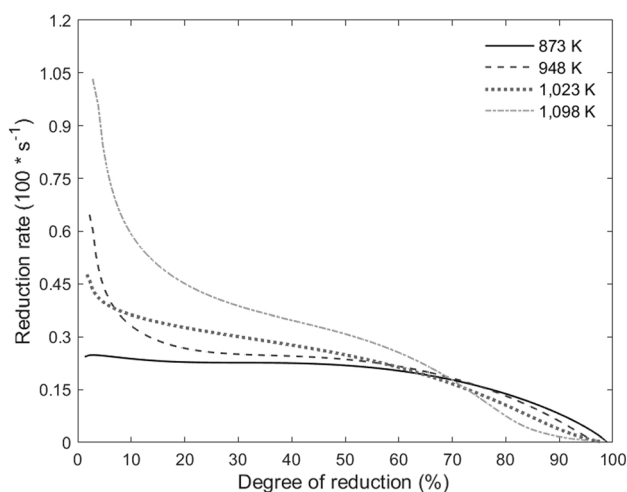


Fig. 6—Comparison of the reduction rate against degree of reduction of the experimental results of the 90 pct oxidized magnetite iron ore ultra-fines.

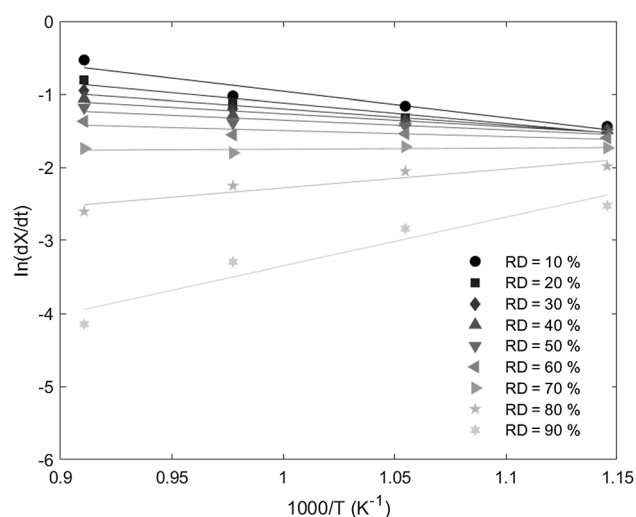


Fig. 7—Arrhenius plot at defined degrees of reduction of the experimental results of the 90 pct oxidized magnetite iron ore ultra-fines.

seen that five of the models fit with $R^2 > 0.97$ and two of them even with $R^2 > 0.99$, whereby both with > 0.99 are nucleation models. Table IV displays all fitting results of the conventional fitting model of the conducted experiments listed. It can be observed that at low reduction temperatures, the nucleation models show a good fit. In contrast, at higher reduction temperatures, a shift away from the nucleation models towards geometrical contraction and diffusion models is given.

Because of several good fits of the experimental data with the conventional models, it is difficult to determine the reaction mechanism.^[39] Several authors have reported a high number of well-fitting models using the conventional model-fitting method.^[6,24,44–49]

B. Multi-Step Kinetic Analysis

A multi-step kinetic analysis, based on the model developed by Johnson–Mehl–Avrami (JMA), was used to identify the mechanism that controls the kinetics during the reduction, given by Eq. [8]^[50–53]:

$$X = 1 - e^{-at^n} \quad [8]$$

where X is the conversion, a is the nucleation rate constant, t the reduction time and n the kinetic exponent. For the identification of the occurring rate-limiting mechanism, the value for the kinetic exponent n is significant. The mechanism is controlled by diffusion for values of n less than 1, by chemical reaction kinetics

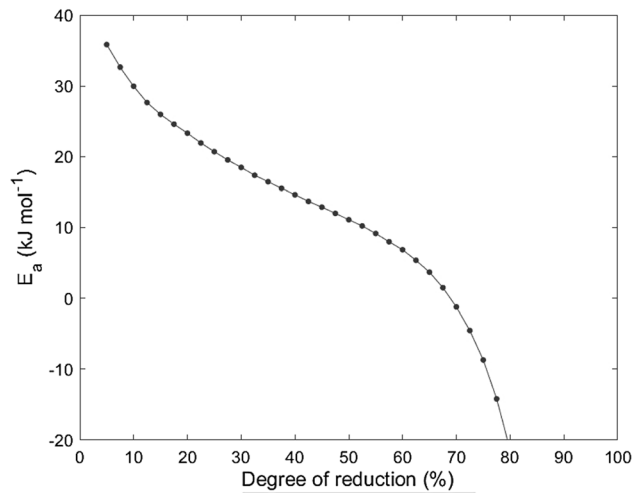


Fig. 8—Apparent activation energy against degree of reduction starting at 5 pct RD of the experimental results of the 90 pct oxidized magnetite iron ore ultra-fines.

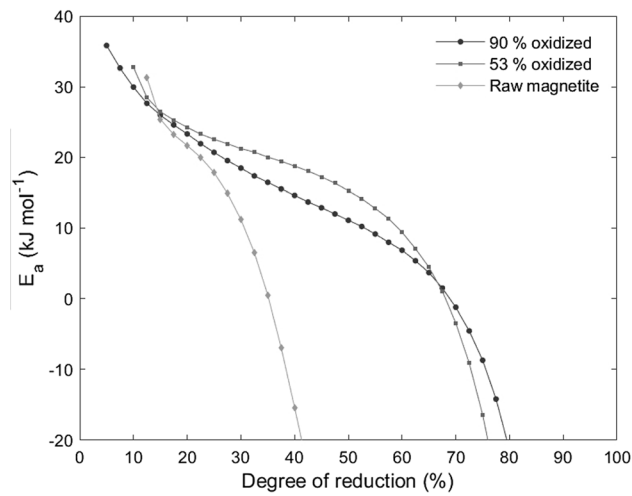


Fig. 9—Comparison of apparent activation energy against degree of reduction of the raw, 53 and 90 pct oxidized magnetite iron ore ultra-fines.

for values of n close to 1, and by nucleation for values greater than 1.5; $n = 1.5$ represents a zero-nucleation rate, between 1.5 and 2.5 represents a decreasing nucleation rate, $n = 2.5$ represents a constant nucleation rate and above 2.5 an increasing nucleation rate.^[24,54,55] According to Eq. [9], rate constant k depends on a and n and can be determined as follows:

$$k = a^{\frac{1}{n}} \quad [9]$$

For the evaluation of more than one controlling mechanism acting in parallel, a combination of three mechanisms, based on Eq. [8], is used^[24,56]:

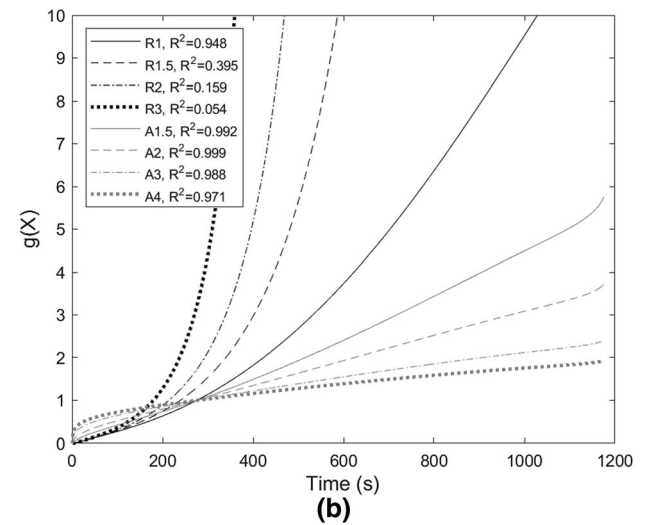
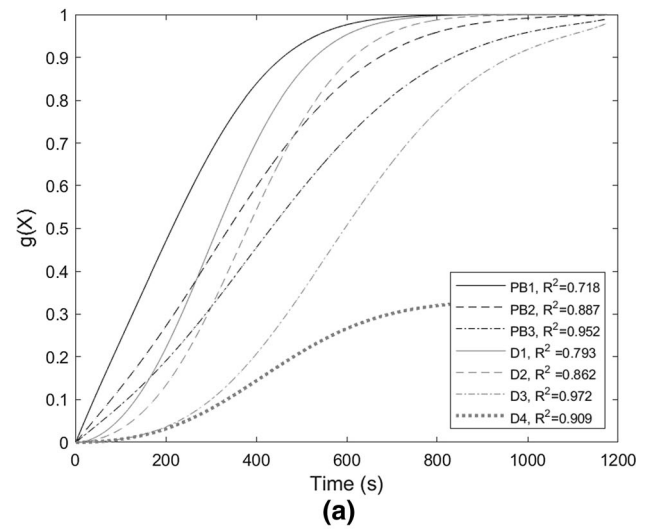


Fig. 10—Conventional model-fitting of the reduction experiment of 90 pct oxidized magnetite with hydrogen at 873 K including R^2 as an indicator for the degree of linearity. (a) PB and D models. (b) R and A models.

$$X_t = X_0 + w_1(1 - e^{-a_1 t^{n_1}}) + w_2(1 - e^{-a_2 t^{n_2}}) + w_3(1 - e^{-a_3 t^{n_3}}) \quad [10]$$

where X_t is the total conversion, X_0 is the initial conversion depending on the input material, and $w_{1,2,3}$, $a_{1,2,3}$ and $n_{1,2,3}$ are the weight factors, nucleation rate constants and kinetic exponents of the three reaction mechanisms, respectively. The sum of the weight factors $w_{1,2,3}$ has to be 1, where 1 represents a complete conversion. For this study, the boundaries for the kinetic exponent are from 1 to 1.15 for n_1 , 0.55 to 0.66 for n_2 and 1.5 to 4 for n_3 in order to clearly differentiate between the reaction mechanisms. The boundaries chosen were checked by applying the conventional model-fitting method to the JMA model from Eq. [8].

Table IV. Coefficient of Determination for the Model-Free Fitting Analysis of the Experimental Data

Model	90.1 Pct OD				53.3 Pct OD				1.8 Pct OD (Raw Magnetite)			
	600	675	750	825	600	675	750	825	600	675	750	825
PB1	0.718	0.670	0.659	0.598	0.861	0.747	0.637	0.697	0.972	0.812	0.834	0.814
PB2	0.888	0.856	0.866	0.836	0.978	0.911	0.842	0.898	0.996	0.951	0.969	0.958
PB3	0.953	0.923	0.936	0.912	0.997	0.962	0.910	0.948	0.976	0.985	0.988	0.975
D1	0.794	0.762	0.765	0.723	0.931	0.834	0.751	0.825	0.984	0.897	0.941	0.941
D2	0.863	0.855	0.871	0.856	0.972	0.910	0.865	0.930	0.959	0.957	0.992	0.993
D3	0.972	0.984	0.993	0.981	0.950	0.987	0.977	0.970	0.818	0.972	0.939	0.918
D4	0.909	0.913	0.931	0.925	0.984	0.951	0.926	0.972	0.929	0.982	0.998	0.994
R1	0.948	0.957	0.953	0.916	0.910	0.961	0.918	0.896	0.811	0.934	0.883	0.854
R1.5	0.396	0.076	0.076	0.047	0.070	0.080	0.041	0.032	0.018	0.052	0.030	0.026
R2	0.160	0.004	0.004	0.003	0.004	0.004	0.003	0.003	0.003	0.003	0.003	0.003
R3	0.054	0.003	0.003	0.003	0.003	0.003	0.003	0.003	0.002	0.003	0.003	0.003
A1	0.992	0.965	0.969	0.934	0.977	0.984	0.932	0.937	0.931	0.982	0.952	0.928
A2	0.999	0.947	0.953	0.916	0.991	0.976	0.911	0.929	0.969	0.981	0.960	0.936
A3	0.988	0.910	0.914	0.874	0.983	0.948	0.866	0.897	0.980	0.955	0.941	0.915
A4	0.972	0.882	0.883	0.841	0.967	0.924	0.832	0.868	0.971	0.929	0.918	0.889

This approach is in the style of the method developed by Hancock and Sharp, which identifies the kinetic exponent by fitting the JMA model to conventional models.^[46,48,57]

The curve-fitting procedure of the experimental results was conducted using MATLAB[®] R2020b by varying $w_{1,2,3}$, $a_{1,2,3}$ and $n_{1,2,3}$ as the fitting parameters. This was in order to minimize the root mean square deviation (RMSD) of the values from the experimental curve x_{exp} and the calculated model x_{calc} , as shown in Eq. [11], where m is the number of data set points^[46]:

$$RMSD = \sqrt{\frac{\sum (x_{calc} - x_{exp})^2}{m - 1}} \quad [11]$$

Various authors have used a similar approach to analyze the limiting mechanisms of the reduction of iron oxides.^[24,44-46,48,55,56,58-60]

Due to the boundaries chosen for the kinetic exponents $n_{1,2,3}$, the fitting proceeds mainly by varying the weight factors $w_{1,2,3}$ between 0 and 1, where the sum of all three is 1, and by varying the nucleation rate constants $a_{1,2,3}$ between 10E-08 and 1. The starting values were varied within the boundaries of the fitting procedure, where the resulting fitting parameters did not vary significantly with different initial choices.

In contrast to the assumptions made for the kinetic expressions, the particles used for the experiments are not monodisperse spheres without impurities. Instead, a particle size distribution with irregularly shaped particles is given with gangue material. In addition, the smaller particles reduce faster compared to bigger particles.^[14,39,48] Consequently, the suggested rate-limiting mechanism for the reduction of iron ores varies among different authors.^[6,49]

Figure 11 shows representative examples of the results from the fitting procedure, using the multi-step kinetic analysis based on the JMA model plotted as degree of reduction, representing the conversion. A similar model

constellation is obtained for raw and both oxidized magnetites for reduction temperatures of 873 K and 948 K, which is illustrated with the raw and 90 pct oxidized magnetite at 873 K in Figures 11(a) and (b), respectively. At low temperatures, the kinetic analysis reveals that the reduction is controlled by chemical reaction at the initial stage. This is indicated by an initially strong increase of the chemical reaction mechanism curve with an n -value of n_1 close to 1. The later stage of the reduction is controlled by nucleation, represented by an increasing course of the nucleation mechanism curve with an n -value of n_2 in the range of 2. The diffusion mechanism, expressed by the dashed line curve with an n -value of n_3 in the range of 0.6, does not contribute to the fit at all. At higher temperatures, the controlling mechanism for the initial and later stages of the reduction of raw magnetite is mainly diffusion. This is illustrated in Figure 11(c) with the dominant course of the diffusion mechanism curve compared to the curves of chemical reaction and nucleation mechanisms. The kinetic limitation changes by a prior oxidation towards a mixture of all three mechanisms at the initial stage, for both 53 and 90 pct OD. This is indicated by a strong increase in all three mechanism curves at the beginning, which is represented by the 90 pct oxidized magnetite in Figure 11(d). For the later stage, the controlling mechanism is diffusion, represented by an increasing course in the diffusion mechanism curve. These findings show a good agreement with those obtained from the conventional model-fitting method. The results from the fitting procedure of the multi-step kinetic analysis for the raw and oxidized magnetites as a function of the temperatures are listed in Table V.

Kuila^[61] reported similar results for the kinetic analysis of the reduction of magnetite ore fines with hydrogen at temperatures of 973 K to 1273 K. The reduction of raw magnetite at higher temperatures follows a limitation by diffusion at the initial and later stages.

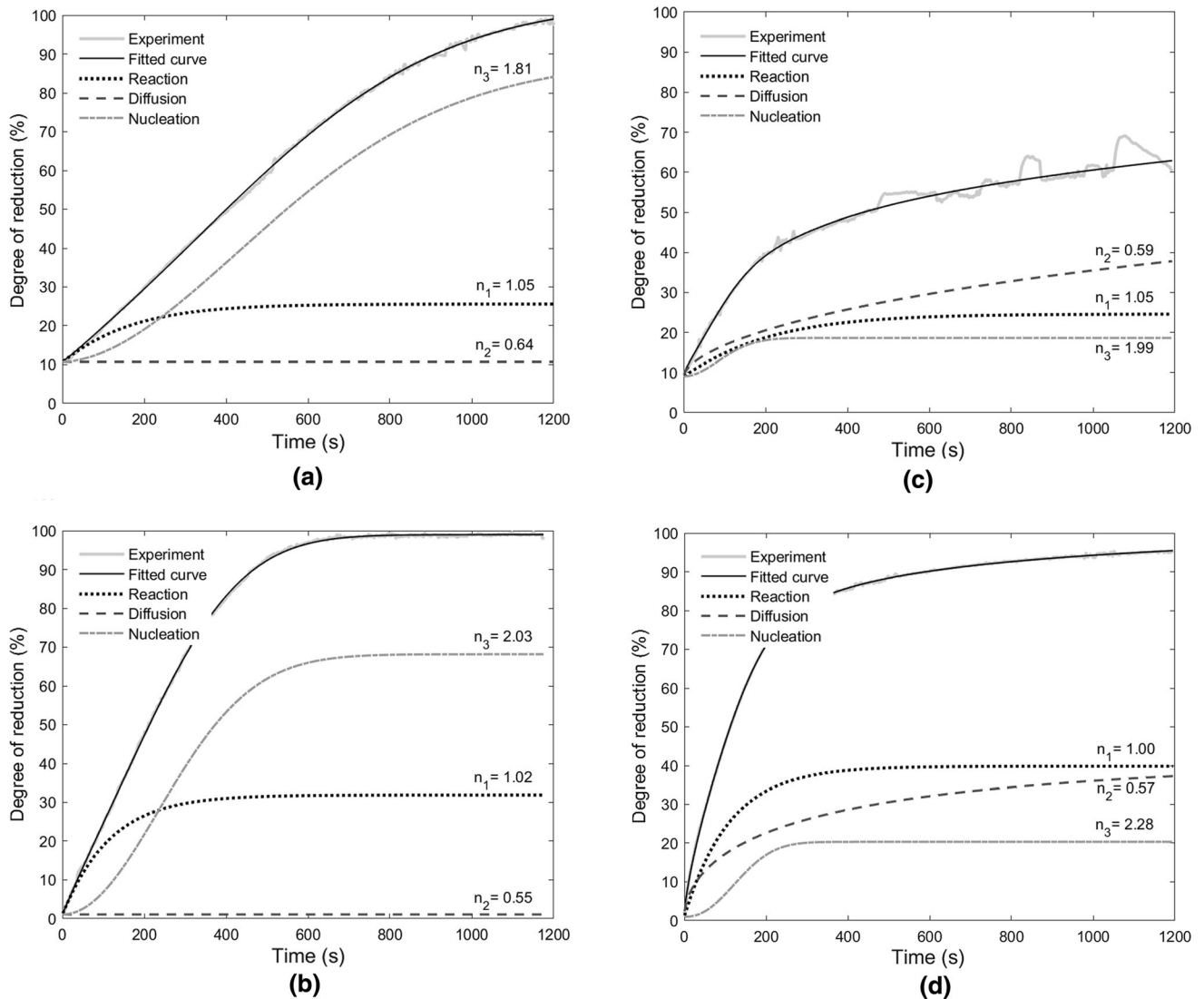


Fig. 11—Fitting results of the multi-step kinetic analysis based on the JMA model at a reduction temperature of 873 K for (a) raw and (b) 90 pct oxidized magnetite and at 1098 K for (c) raw and (d) 90 pct oxidized magnetite.

Using a similar kinetic analyzing method, but a fluidized bed reactor as the testing facility and a hematite-based iron ore with a particle size distribution between 250 and 500 μm , Spreitzer and Schenk identified comparable results for the initial stage of the reduction with hydrogen. At low reduction temperatures, the initial stage of the reduction proceeds correspondingly to chemical reaction, which changes towards diffusion for higher temperatures. For the final stage, different limiting mechanisms were reported, a possible reason for this being the limitation of the gas flow in the fluidized bed and the thermodynamic aspects according to the Baur–Glässner diagram in Figure 3.^[24]

Kim^[15] analyzed the formation of iron morphologies in regard to the limiting kinetic steps for the hydrogen-based reduction of magnetite compacts made of a magnetite powder with particles < 100 μm in size in a temperature range of 773 K to 1273 K. They observed that for high reduction temperatures, a change in the kinetic limitation from a mixture of gaseous mass

transport and interfacial chemical reaction to solid-state diffusion of oxygen occurs. For low reduction temperatures, no change occurs and therefore no retardation of the reduction progress, either. This was confirmed by a porous iron morphology for low and a dense iron morphology for high reduction temperatures. These findings are in line with the results of this study as well as with the work of Fruehan.^[14] He found that the retardation of the hydrogen-based reduction progress is due to the formation of a dense iron shell around the wüstite grains, which results in a limitation by oxygen diffusion through iron.

V. MORPHOLOGICAL ANALYSIS

To confirm the results of a kinetic study, a straightforward approach in the field of iron ore reduction is to analyze the morphology of the reduced samples.^[6,14,15,24] Figures 12 and 13 show the polished

Table V. Fitting Parameters of the Multi-Step Kinetic Analysis

	Pct OD	a_1 (-)	a_2 (-)	a_3 (-)	n_1 (-)	n_2 (-)	n_3 (-)	k_1 (s ⁻¹)	k_2 (s ⁻¹)	k_3 (s ⁻¹)	w_1 (Pct)	w_2 (Pct)	w_3 (Pct)	RMSD (-)
873 K	90.1	7.68E-03	1.58E-07	7.82E-06	1.02	0.56	2.03	8.63E-03	5.98E-13	3.05E-03	30.80	2.11	67.09	3.72E-03
	53.3	5.82E-03	9.67E-03	8.45E-06	1.00	0.57	1.91	5.82E-03	2.75E-04	2.21E-03	30.86	9.36	59.77	5.65E-03
	1.8	4.50E-03	3.94E-06	7.75E-06	1.06	0.65	1.81	5.99E-03	4.80E-09	1.51E-03	14.87	7.53	77.60	4.99E-03
948 K	90.1	6.48E-03	3.58E-02	1.59E-05	1.05	0.60	1.98	8.40E-03	3.87E-03	3.74E-03	19.62	29.01	51.38	5.25E-03
	53.3	6.75E-03	2.12E-02	1.08E-05	1.02	0.55	1.96	7.53E-03	9.08E-04	2.90E-03	32.81	17.08	50.11	2.69E-03
1023 K	1.8	2.26E-03	2.20E-03	2.62E-05	1.04	0.66	1.82	2.85E-03	9.30E-05	3.02E-03	36.20	13.78	50.02	3.96E-03
	90.1	5.34E-03	2.33E-02	2.00E-05	1.00	0.58	1.99	5.35E-03	1.59E-03	4.37E-03	61.71	14.09	24.20	5.00E-03
1098 K	53.3	8.67E-03	2.19E-02	4.98E-05	1.05	0.57	1.87	1.11E-02	1.26E-03	5.00E-03	11.60	37.91	50.49	1.15E-02
	1.8	2.67E-03	6.36E-03	4.00E-05	1.05	0.60	2.10	3.62E-03	2.16E-04	8.12E-03	41.73	55.46	2.82	2.94E-03
1098 K	90.1	8.98E-03	3.55E-02	9.63E-06	1.00	0.57	2.28	8.99E-03	2.88E-03	6.38E-03	38.84	41.80	19.36	2.35E-03
	53.3	8.63E-03	2.27E-02	1.90E-05	1.00	0.58	2.06	8.64E-03	1.47E-03	5.10E-03	26.54	53.67	19.79	2.19E-03
1.8	3.65E-03	6.94E-03	7.30E-05	1.05	0.60	1.99	4.86E-03	2.50E-04	8.40E-03	15.53	74.90	9.57	1.30E-02	

microsections after reduction and at a degree of reduction of approximately 50 pct, respectively, obtained from the reduction at 873 K and 1098 K. The iron appears white and the remaining wüstite gray. In the case of a low reduction temperature, the type of iron morphology formed is highly porous for both raw and oxidized magnetites, as given in Figures 12(a) through (c). Thus, pre-oxidation of the magnetite has no significant influence at low reduction temperatures. The nucleation points for the formation of the first iron are mainly at the surface of the dense wüstite particles for both raw and oxidized magnetites, as shown in Figures 13(a) through (c). In the case of higher reduction temperatures, a prior oxidation of the magnetite changes the iron morphology obtained from a dense iron layer around a dense wüstite core to many small coarsely porous wüstite cores with a dense iron layer, as exhibited in Figures 12(d) through (f). For the raw magnetite, the first iron is only formed at the surface of the dense wüstite particles, which can be observed in Figure 13(d). In comparison to both oxidized magnetites, illustrated in Figures 13(e) and (f), the nucleation points of the first iron are evenly distributed in the coarsely porous wüstite particles.

According to literature, for the reduction of iron oxides, three different types of iron morphologies, porous, dense and fibrous (whisker), as well as a mixture, have been observed.^[17,62,63] The type of iron morphology depends not only on the process conditions such as temperature and gas composition, but also on the characteristics of the iron oxide.^[17,27,28,63]

Focusing on the hydrogen-based reduction, several authors have reported that gases containing high amounts of hydrogen lead to a porous iron growth.^[64–68] By increasing the amount of H₂O in the reducing gas, some authors^[14,15,63–68] have identified porous and dense iron as a layer around the remaining wüstite, but no whisker at all. In contrast, Moujahid and Rist^[28] and Gransden and Sheasby^[69] reported the formation of iron whisker for hydrogen/water vapor gas mixtures, whereas Gransden and Sheasby also found iron whisker for the reduction with pure hydrogen.^[28,69] St. John *et al.*^[62,64,66] claimed that the breakdown of the dense iron layer, due to the bursting of the gaseous reaction product H₂O, is a prerequisite for the porous iron morphology for the hydrogen-based reduction of wüstite. However, this theory is not supported by Moujahid and Rist.^[28] Moujahid and Rist^[28] as well as Nicolle and Rist^[63] found that in order to obtain a porous iron morphology, the relationship between the process conditions and nuclei sites of the iron oxide is critical, which is supported by the findings in this study. The reduction mechanism for the reduction of Fe₂O₃ to Fe with hydrogen proceeds at temperatures above 843 K of *via* Fe₃O₄ and FeO, according to thermodynamic calculations. For a porous iron morphology, a low reduction rate at the initial stage of the reduction is required to avoid an iron ion built-up in the wuestite, which is given for a limitation due to chemical reaction. Thus, the generated amount of iron ions fits to the number of nuclei sites. At increased temperatures the reduction rate increases and an iron ion built-up in the

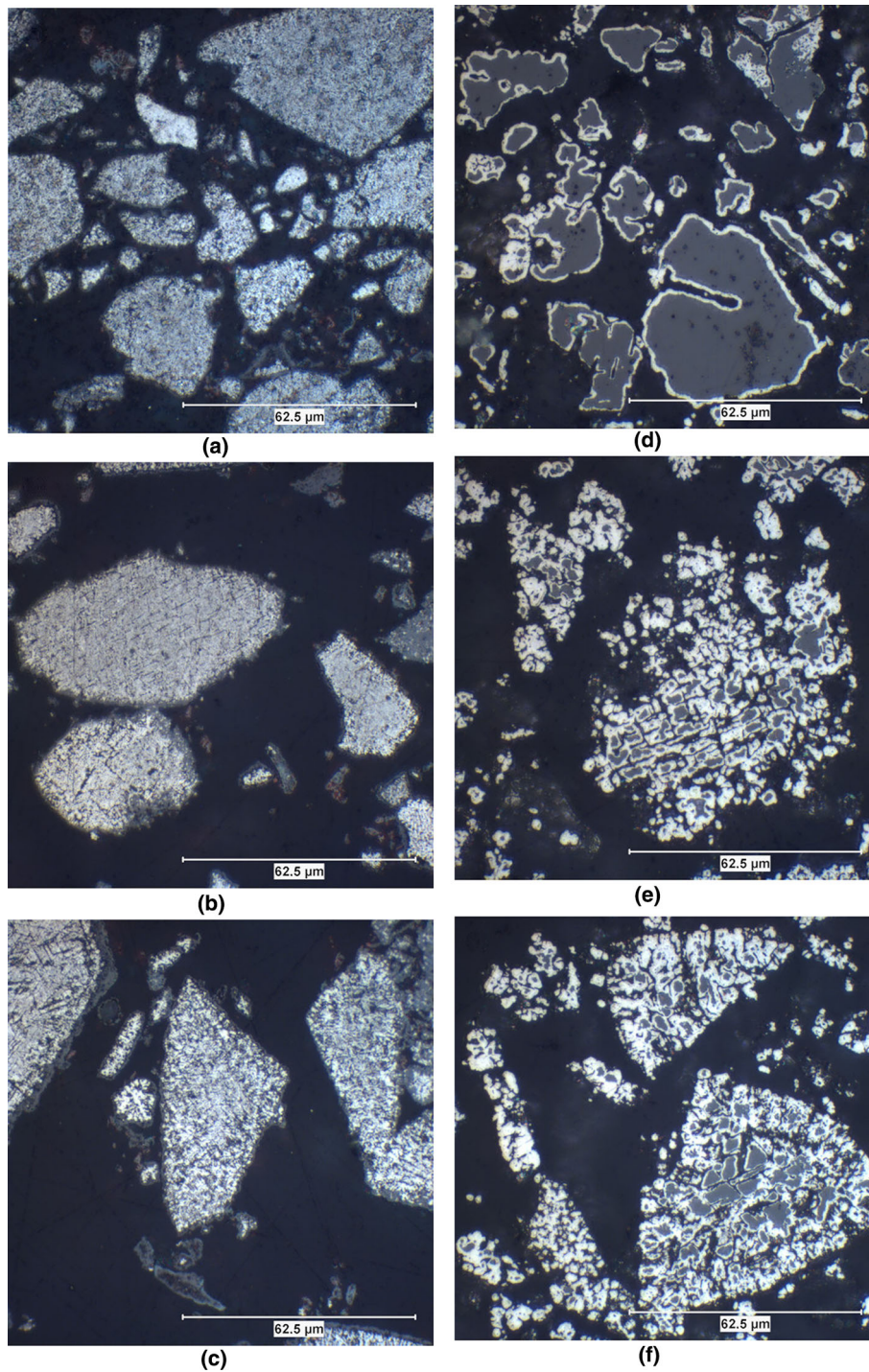


Fig. 12—Polished microsections after the reduction with hydrogen at a reduction temperature of 873 K for (a) raw; (b) 53 pct; (c) 90 pct and at 1098 K for (d) raw; (e) 53 pct; (f) 90 pct.

wuestite occurs, which is given a limitation due to diffusion. In combination with less preferred nuclei sites, too many iron ions are generated compared to the nuclei sites, which leads to a dense iron shell. The oxidized samples showing magnetite particles covered with hematite and hematite needles inside the particle. As

mentioned, the reduction of the hematite proceeds at first, which has to affect the number of nuclei sites for the iron ions, as illustrated in Figure 13(e) and (f).

The findings in this study show that a porous iron morphology is achieved when the reduction proceeds mainly corresponding to the chemical reaction mechanism at the initial stage, given at low reduction temperatures of 873 K and 948 K for both raw and

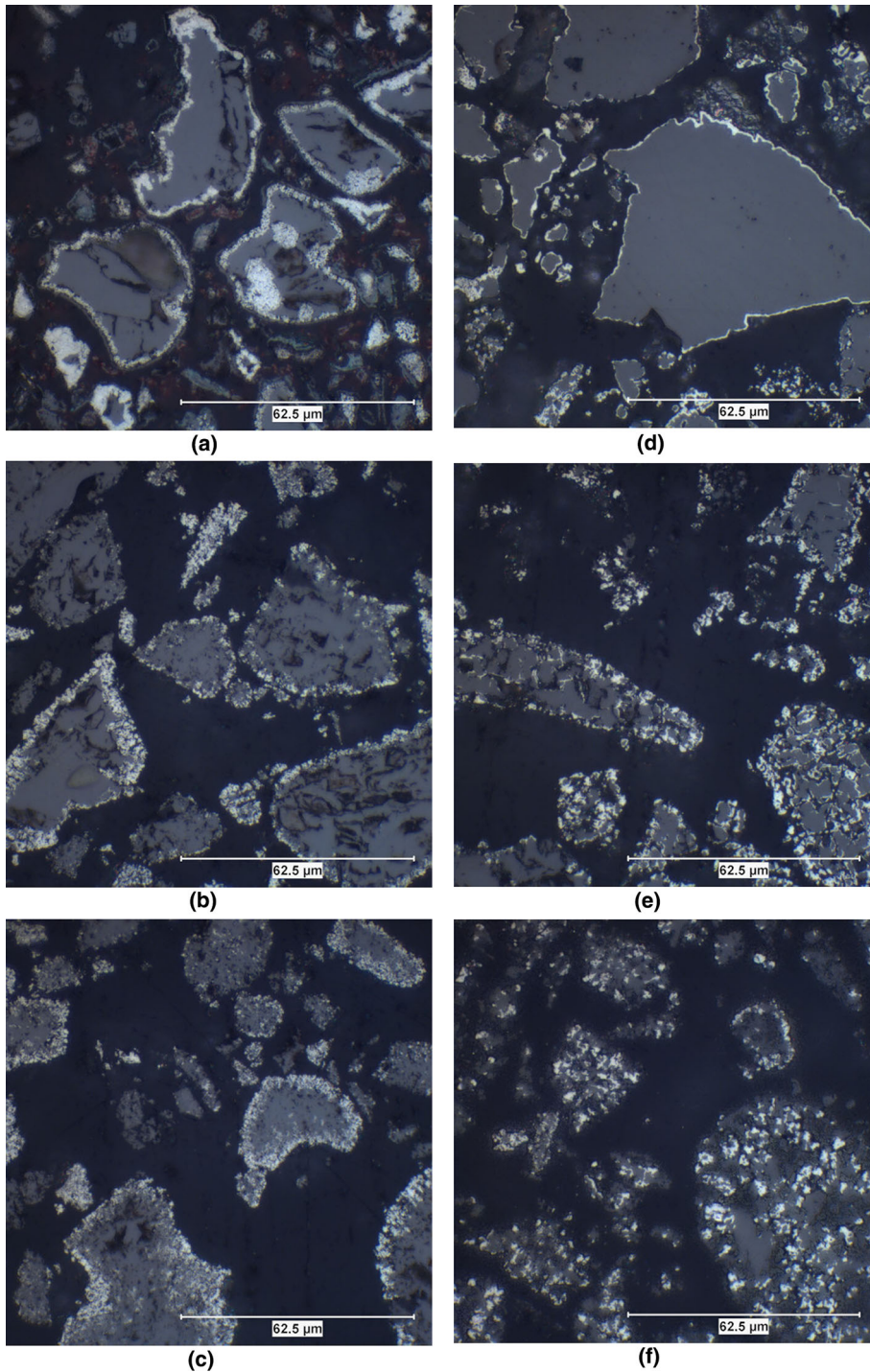


Fig. 13—Polished microsections at appr. 50 pct RD reduced with hydrogen at a reduction temperature of 873 K for (a) raw; (b) 53 pct; (c) 90 pct and at 1098 K for (d) raw; (e) 53 pct; (f) 90 pct.

oxidized magnetite ultra-fine iron ores. The work of Kim *et al.*^[15] confirms the results presented in this study for the reduction of magnetite with hydrogen at given temperatures. Matthew and Hayes^[66,67] found porous iron for the reduction of magnetite with hydrogen at similar low reduction temperatures. At increased reduction temperatures of 1023 K and 1098 K, the effect of a prior oxidation leads to a change in the kinetic

limitation. The change is given at the initial reduction stage from mainly diffusion controlled for raw magnetite to mixed controlled for oxidized magnetite, thus changing the iron morphology. According to Edström,^[27] this kinetic transformation is because of the coarsely porous wüstite obtained during the reduction of oxidized magnetites. The iron morphology is dense for both raw and oxidized magnetites, but instead of a dense

wüstite, a coarsely porous wüstite is given for the oxidized magnetites, as seen in Figures 13(e) and (f). As a result, the kinetic limitation is different for the initial reduction stage and similar for the final reduction stage. According to Nicolle and Rist,^[63] the controlling mechanism for dense iron is at the initial stage of the reduction diffusion. This means that due to the reduction process on the outer surface, the inward transport of iron ions from the surface is negligible compared to the generation of iron ions. Therefore, the iron ion build-up at the surface leads to a dense iron layer, resulting in the retardation of the reduction due to the limitation of diffusion through the dense iron layer.

VI. CONCLUSIONS

The influence of pre-oxidation on the reduction behavior of magnetite ultra-fine iron ores by means of kinetics and iron morphology was investigated using hydrogen as reducing agent at temperatures from 873 to 1098 K in a thermogravimetric analyzer. The apparent activation energy was studied according to the model-free method as a function of the degree of reduction. The kinetic analysis was performed by two methods: the conventional model-fitting method and the multi-step method, based on the Johnson–Mehl–Avrami model, to determine the limiting mechanism during reduction. The results of the kinetic analysis were checked by the morphology of the iron formed using polished micro-sections. The following conclusions can be drawn:

1. The reducibility of magnetite ultra-fines is significantly favored by a prior oxidation, especially at higher reduction temperatures. The higher the oxidation degree, the higher the reduction rate.
2. At a moderate reduction temperature of 948 K, a minimum effect for both the influence of the oxidation and the required time to reach a degree of reduction of 95 pct were found.
3. The apparent activation energies show negative values for both raw and oxidized magnetite ultra-fines due to the faster reduction at lower temperatures, depending on the degree of reduction. The pre-oxidation delays the point of RD at which the apparent activation energy turns negative.
4. The controlling mechanisms are observed to vary with a prior oxidation and with temperature. At low reduction temperatures of 873 K and 948 K, the reduction is limited mainly by chemical reaction for the initial stage and by nucleation for the final stage, for both raw and oxidized magnetite iron ore ultra-fines. The reduction of raw magnetite at higher temperatures, 1023 K and 1098 K, is mainly controlled by diffusion, for both the initial and later stages. Oxidized magnetite reduced at these temperatures is mixed-controlled at the initial stage, but still diffusion-controlled for the later stage.
5. Morphological analysis confirms the kinetic evaluation. Porous iron morphology is formed at low reduction temperatures of 873 K and 948 K for both raw and oxidized magnetite iron ore ultra-fines. A

dense iron layer around a remaining dense wüstite core is formed for the reduction of raw magnetite at higher temperatures, 1023 K and 1098 K. Many small coarsely porous wüstite cores with a dense iron layer are also formed for the reduction of oxidized magnetite at these temperatures.

6. For a hydrogen-based direct reduction technology to process magnetite iron ore ultra-fines, lower reduction temperatures and a prior oxidation are recommended, whereby a high degree of oxidation is not necessary.

ACKNOWLEDGMENTS

The authors gratefully acknowledge the funding support of K1-MET GmbH, metallurgical competence center. The research program of the K1-MET competence center is supported by COMET (Competence Center for Excellent Technologies), the Austrian program for competence centers. COMET is funded by the Federal Ministry for Climate Action, Environment, Energy, Mobility, Innovation and Technology, the Federal Ministry for Digital and Economic Affairs, the Federal States of Upper Austria, Tyrol and Styria as well as the Styrian Business Promotion Agency (SFG) and the Standortagentur Tyrol. Furthermore, we thank Upper Austrian Research GmbH for the continuous support. Besides the public funding from COMET, this research project is partially financed by the industrial partners Primetals Technologies Austria GmbH.

CONFLICT OF INTEREST

On behalf of all authors, the corresponding author states that there is no conflict of interest.

FUNDING

Open access funding provided by Montanuniversität Leoben.

OPEN ACCESS

This article is licensed under a Creative Commons Attribution 4.0 International License, which permits use, sharing, adaptation, distribution and reproduction in any medium or format, as long as you give appropriate credit to the original author(s) and the source, provide a link to the Creative Commons licence, and indicate if changes were made. The images or other third party material in this article are included in the article's Creative Commons licence, unless indicated otherwise in a credit line to the material. If material is not included in the article's Creative Commons licence and your intended use is not permitted by statutory

regulation or exceeds the permitted use, you will need to obtain permission directly from the copyright holder. To view a copy of this licence, visit <http://creativecommons.org/licenses/by/4.0/>.

REFERENCES

1. M. Fishedick, J. Marzinkowski, P. Winzer, and M. Weigel: *J. Clean. Prod.*, 2014, vol. 84, pp. 563–80.
2. A. Hasanbeigi, M. Arens, and L. Price: *Renew. Sustain. Energy Rev.*, 2014, vol. 33, pp. 645–58.
3. V. Vogl, M. Åhman, and L.J. Nilsson: *J. Clean. Prod.*, 2018, vol. 203, pp. 736–45.
4. K. Rechberger, A. Spanlang, A. Sasiain Conde, H. Wolfmeir, and C. Harris: *Steel Res. Int.*, 2020, vol. 91, pp. 1–10.
5. M. Kirschen, K. Badr, and H. Pfeifer: *Energy*, 2011, vol. 36, pp. 6146–55.
6. A. Pineau, N. Kanari, and I. Gaballah: *Thermochim. Acta*, 2007, vol. 447, pp. 75–88.
7. A.M. Nyembwe, R.D. Cromarty, and A.M. Garbers-Craig: *Powder Technol.*, 2016, vol. 295, pp. 7–15.
8. C.C. Xu and D-Q. Cang: *J. Iron Steel Res. Int.*, 2010, vol. 17, pp. 1–7.
9. J.L. Schenk: *Particuology*, 2011, vol. 9, pp. 14–23.
10. F.J. Plaul, C. Böhm, J.L. Schenk: *J. South. Afr. Inst. Min. Metall.*, 2009, pp. 121–28.
11. D. Nuber, H. Eichberger, B. Rollinger: *Stahl Eisen*, 2006, pp. 47–51.
12. R. Lucena, R. Whipp, and W. Abarran: *Stahl Eisen*, 2007, vol. 127, pp. 67–80.
13. C. Thaler, T. Tappeiner, J.L. Schenk, W.L. Kepplinger, J.F. Plaul, and S. Schuster: *Steel Res. Int.*, 2012, vol. 83, pp. 181–88.
14. R.J. Fruehan, Y. Li, L. Brabie, and E-J. Kim: *Scand. J. Metall.*, 2005, vol. 34, pp. 205–12.
15. W-H. Kim, S. Lee, S-M. Kim, and D-J. Min: *Int. J. Hydrogen Energy*, 2013, vol. 38, pp. 4194–200.
16. S. Hayashi and Y. Iguchi: *ISIJ Int.*, 1992, vol. 32, pp. 962–71.
17. H.W. Gudenau, J. Fang, T. Hirata, and U. Gebel: *Steel Res. Int.*, 1989, vol. 60, pp. 138–44.
18. S. He, H. Sun, C. Hu, J. Li, Q. Zhu, and H. Li: *Powder Technol.*, 2017, vol. 313, pp. 161–68.
19. S.Y. Ezz: *Trans. Metall. Soc. AIME*, 1960, vol. 218, pp. 709–15.
20. B.G. Langston, F.M. Stephens: *J. Met.*, 1960, pp. 312–16.
21. Y. Zhong, Z. Wang, Z. Guo, and Q. Tang: *Powder Technol.*, 2014, vol. 256, pp. 13–19.
22. X. Gong, B. Zhang, Z. Wang, and Z. Guo: *Metall. Mater. Trans. B*, 2014, vol. 45B, pp. 2050–56.
23. L. Guo, Q. Bao, J. Gao, Q. Zhu, and Z. Guo: *ISIJ Int.*, 2020, vol. 60, pp. 1–17.
24. D. Spreitzer and J.L. Schenk: *Metall. Mater. Trans. B*, 2019, vol. 50B, pp. 2471–84.
25. X.J. Wang, R. Liu, and J. Fang: *AMR*, 2012, vols. 482–484, pp. 1354–57.
26. H. Zheng, D. Spreitzer, T. Wolfinger, J. Schenk, and R. Xu: *Metall. Mater. Trans. B*, 2021, vol. 52B, pp. 1955–71.
27. J.O. Edström: *J. Iron Steel Inst.*, 1953, pp. 289–304.
28. S.E. Moujahid and A. Rist: *Metall. Trans. B*, 1988, vol. 19, pp. 787–802.
29. S. Song and P.C. Pistorius: *ISIJ Int.*, 2019, vol. 59, pp. 1765–69.
30. A. Pichler, H. Mali, J.F. Plaul, J. Schenk, M. Skorianz, B. Weiss: *Steel Res. Int.*, 2016, pp. 642–49.
31. B. Weiss, J. Sturn, S. Voglsam, S. Strobl, H. Mali, F. Winter, and J. Schenk: *Ironmak. Steelmak.*, 2011, vol. 38, pp. 65–73.
32. M. Skorianz, H. Mali, A. Pichler, F. Plaul, J. Schenk, and B. Weiss: *Steel Res. Int.*, 2016, vol. 87, pp. 633–41.
33. B. Weiss, J. Sturn, S. Voglsam, S. Strobl, H. Mali, F. Winter, and J. Schenk: *Steel Res. Int.*, 2010, vol. 81, pp. 93–99.
34. H.J. Cho, M. Tang, and P.C. Pistorius: *Metall. Mater. Trans. B*, 2014, vol. 45B, pp. 1213–20.
35. T.K. Sandeep Kumar, N.N. Viswanathan, H. Ahmed, A. Dahlin, C. Andersson, and B. Bjorkman: *Metall. Mater. Trans. B*, 2019, vol. 50B, pp. 150–61.
36. H. Zheng, J. Schenk, D. Spreitzer, T. Wolfinger, and O. Daghighaleh: *Steel Res. Int.*, 2021, vol. 92, p. 2000687.
37. S.P.E. Forsmo, S.-E. Forsmo, P.-O. Samskog, and B.M.T. Björkman: *Powder Technol.*, 2008, vol. 183, pp. 247–59.
38. L. von Bogdandy and H.-J. Engell: *The Reduction of Iron Ores*, Springer-Verlag, Berlin Heidelberg GmbH, Düsseldorf, 1971, pp. 18–38.
39. A. Khawam and D.R. Flanagan: *J. Phys. Chem. B*, 2006, vol. 110, pp. 17315–28.
40. P. Simon: *J. Therm. Anal. Calorim.*, 2004, vol. 76, pp. 123–32.
41. M. Pjolat, L. Favregeon, M. Soustelle: *Thermochim. Acta*, 2011, pp. 93–102.
42. T. Ozawa: *Thermochim. Acta*, 1992, vol. 203, pp. 159–65.
43. D. Spreitzer and J. Schenk: *Particuology*, 2020, vol. 52, pp. 36–46.
44. H. Chen, Z. Zheng, Z. Chen, and X.T. Bi: *Powder Technol.*, 2017, vol. 316, pp. 410–20.
45. H. Chen, Z. Zheng, Z. Chen, W. Yu, and J. Yue: *Metall. Mater. Trans. B*, 2017, vol. 48B, pp. 841–52.
46. K. Piotrowski, K. Mondal, H. Lorethova, L. Stonawski, and T. Wiltowski: *Int. J. Hydrogen Energy*, 2005, vol. 30, pp. 1543–54.
47. M.H. Jeong, D.H. Lee, and J.W. Bae: *Int. J. Hydrogen Energy*, 2015, vol. 40, pp. 2613–20.
48. K. Piotrowski, K. Mondal, T. Wiltowski, P. Dydo, and G. Rizog: *Chem. Eng. J.*, 2007, vol. 131, pp. 73–82.
49. P. Pourghahramani and E. Forsberg: *Thermochim. Acta*, 2007, vol. 454, pp. 69–77.
50. M. Avrami: *J. Chem. Phys.*, 1939, vol. 7, pp. 1103–12.
51. M. Avrami: *J. Chem. Phys.*, 1940, vol. 8, pp. 212–24.
52. M. Avrami: *J. Chem. Phys.*, 1941, vol. 9, pp. 177–84.
53. W.A. Johnson and R.F. Mehl: *Trans. Metall. Soc. AIME*, 1939, vol. 135, pp. 416–58.
54. J. Málek: *Thermochim. Acta*, 1995, vol. 267, pp. 61–73.
55. E.R. Monazam, R.W. Breault, and R. Siriwardane: *Chem. Eng. J.*, 2014, vol. 242, pp. 204–210.
56. E.R. Monazam, R.W. Breault, R. Siriwardane, and D.D. Miller: *Ind. Eng. Chem. Res.*, 2013, vol. 52, pp. 14808–16.
57. J.D. Hancock and J.H. Sharp: *J. Am. Ceram. Soc.*, 1972, vol. 55, pp. 74–77.
58. Y. Kapelyushin, Y. Sasaki, J. Zhang, S. Jeong, and O. Ostrovski: *Metall. Mater. Trans. B*, 2016, vol. 47B, pp. 2263–78.
59. R.W. Breault and E.R. Monazam: *Energy Technol.*, 2016, vol. 4, pp. 1221–29.
60. E.R. Monazam, R.W. Breault, R. Siriwardane, G. Richards, and S. Carpenter: *Chem. Eng. J.*, 2013, vol. 232, pp. 478–87.
61. S.K. Kuila, R. Chatterjee, and D. Ghosh: *Int. J. Hydrogen Energy*, 2016, vol. 41, pp. 9256–66.
62. D.H. St. John, S.P. Matthew, and P.C. Hayes: *Metall. Trans. B*, 1984, vol. 15, pp. 709–17.
63. R. Nicolle and A. Rist: *Metall. Trans. B*, 1979, vol. 10, pp. 429–38.
64. D.H. St. John, S.P. Matthew, and P.C. Hayes: *Metall. Trans. B*, 1984, vol. 15, pp. 701–08.
65. D.H. St. John and P.C. Hayes: *Metall. Trans. B*, 1982, vol. 13, pp. 117–24.
66. S.P. Matthew, T.R. Cho, and P.C. Hayes: *Metall. Trans. B*, 1990, vol. 21, pp. 733–41.
67. S.P. Matthew and P.C. Hayes: *Metall. Trans. B*, 1990, vol. 21, pp. 153–72.
68. E.T. Turkdogan and J.V. Vinters: *Metall. Mater. Trans. B*, 1971, vol. 2B, pp. 3175–88.
69. J.F. Gransden and J.S. Sheasby: *Can. Metall. Q.*, 1974, vol. 13, pp. 649–57.

Publisher's Note Springer Nature remains neutral with regard to jurisdictional claims in published maps and institutional affiliations.